Inorganic Chemistry

Article

pubs.acs.org/IC

X-ray Absorption and Emission Study of Dioxygen Activation by a Small-Molecule Manganese Complex

Julian A. Rees,[†,‡] Vlad Martin-Diaconescu,[†] Julie A. Kovacs,*[,‡] and Serena DeBeer*[,†,§]

[†]Max-Planck-Institut für Chemische Energiekonversion, Stiftstrasse 34-36, Mülheim an der Ruhr D-45470, Germany

[‡]Department of Chemistry, University of Washington, Box 351700, Seattle, Washington 98195-1700, United States

[§]Department of Chemistry and Chemical Biology, Cornell University, Ithaca, New York 14853, United States

Supporting Information

ABSTRACT: Manganese K-edge X-ray absorption (XAS) and Kβ emission (XES) spectroscopies were used to investigate the factors contributing to O−O bond activation in a small-molecule system. The recent structural characterization of a metastable peroxo-bridged dimeric $Mn(III)_2$ complex derived from dioxygen has provided the first opportunity to obtain X-ray spectroscopic data on this type of species. Ground state and time-dependent density functional theory calculations have provided further insight into the nature of the transitions in XAS pre-edge and valence-to-core (VtC) XES spectral regions. An experimentally validated electronic structure description has also enabled the determination of structural and electronic factors that govern peroxo bond activation, and have allowed us to propose both a rationale for the metastability of this unique compound, as well as potential future ligand designs which may further promote or inhibit O−O bond scission. Finally, we have explored the potential of VtC XES as an element-selective probe of both the coordination mode and degree of activation of peroxomanganese adducts. The comparison of these results to a recent VtC XES study of iron-mediated dintrogen activation helps to illustrate the factors that may determine the success of this spectroscopic method for future studies of small-molecule activation at transition metal sites.

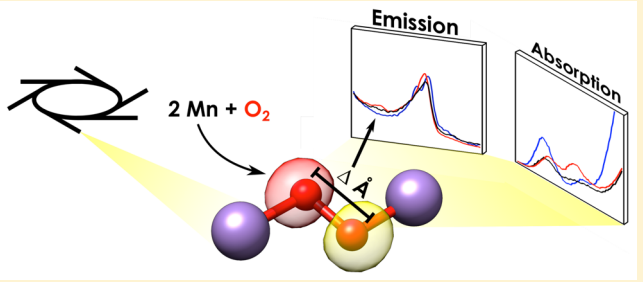

INTRODUCTION

Molecular oxygen is a benign yet highly competent oxidant, and its natural abundance has led to widespread incorporation into both industrial and biological catalysis.[1−4] Despite an often large thermodynamic driving force, oxidative transformations using dioxygen involve a significant obstacle: activation of the strong O=O bond.[5,6] Nature has evolved efficient catalysts for O_2 activation in the form of metalloenzymes, many of which contain manganese ions as essential cofactors. Not only are manganese metalloenzymes involved in the activation and reduction of O_2 (Mn ribonucleotide reductase, Mn lipoxygenase)[7−12] and its more harmful reduced derivatives (Mn superoxide dismutase, Mn catalase),[13,14] but nature also exclusively utilizes manganese as the redox-active metal involved in dioxygen formation from water, carried out at the Mn_4Ca cluster of Photosystem II (PSII).[2,15,16]

Despite the critical role of Mn in both biological O_2 activation and formation, fundamental understanding of these processes is far from complete. Biomimetic small-molecule chemistry continues to play a key role in furthering mechanistic insight into enzymatic small-molecule activation. Recent prior work has resulted in the observation of a novel intermediate formed via the reaction of the Mn(II) complex $[Mn^{II}(S^{Me2}$(6-Me-DPEN))]$^+$ (**1**) with molecular oxygen.[17,18] This metastable intermediate was identified as a $Mn(III)_2$ peroxo-bridged dimer, $\{[Mn^{III}(S^{Me2}$(6-Me-DPEN))$]_2$(*trans*-μ-1,2-O_2)$\}^{+2}$ (**2**), which forms en route to a stable mono-oxo-bridged $Mn(III)_2$ final product $\{[Mn^{III}(S^{Me2}$(6-Me-DPEN))$]_2(\mu$-O)$\}^{+2}$ (**3**) (Scheme 1). The peroxo unit in **2** was shown to coordinate in a *trans* μ-1,2 fashion, and this complex was characterized by X-ray crystallography, stopped-flow UV−vis and resonance Raman spectroscopies, and SQUID magnetometry. The conversion of **1** to **3** via **2** is quantitative, and an O−O bond length of 1.452(5) Å indicates that the O−O bond in **2** is highly activated. Finally, experiments conducted with $^{18}O_2$ have provided definitive proof that both the peroxo and oxo bridges are dioxygen-derived.[17]

We have also previously reported a series of structurally characterized monomeric Mn(III)-alkylperoxo complexes using derivatives of this same DPEN ligand scaffold.[19] Variation in the peroxo bond length was found to correlate with the Mn(III)-N-heterocyclic amine distance, indicating that these ligands *cis* to the peroxo play an important role in mediating O−O bond activation. Theoretical investigation of these compounds revealed that the Mulliken charge, or Lewis acidity, of the Mn(III) ion can be tuned by the N-heterocyclic amine distance, and these changes affect the degree of peroxo bond activation. Decreased Lewis acidity was found to result in less Mn d character in the peroxo π_v* orbital (the peroxo π* orbital

Received: April 2, 2015
Published: June 10, 2015

DOI: 10.1021/acs.inorgchem.5b00699
Inorg. Chem. 2015, 54, 6410−6422

Scheme 1. Dioxygen Reactivity of $[Mn^{II}(S^{Me2}N_4(6\text{-Me-DPEN}))]^+$ (1) Showing Formation of Metastable $\{[Mn^{III}(S^{Me2}N_4(6\text{-Me-DPEN}))]_2(\textit{trans-}\mu\text{-}1,2\text{-}O_2)\}^{2+}$ (2) and Conversion to Final Product $\{[Mn^{III}(S^{Me2}N_4(6\text{-Me-DPEN}))]_2(\mu\text{-}O)\}^{2+}$ (3)

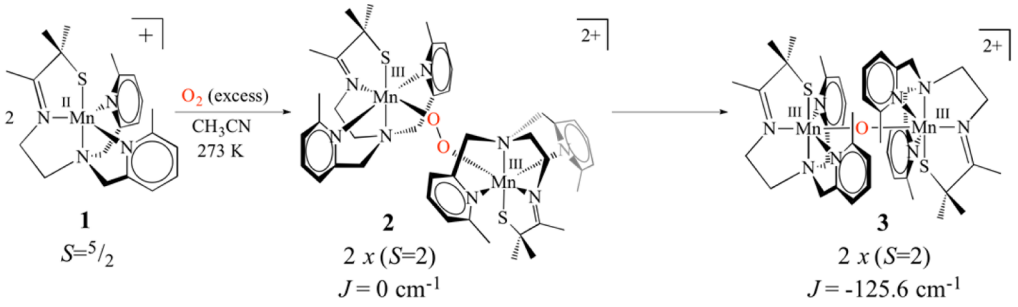

perpendicular to the Mn−O−O plane), and a longer O−O bond. As shown in Figure 1, the metrical parameters for the peroxo dimer **2** appear to closely follow this correlation, suggesting that the same structural and electronic effects are present in this system.

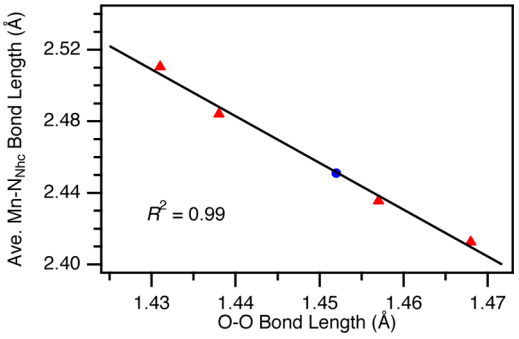

Figure 1. Plot of O−O bond length (Å) vs average Mn(III)-N-hetercycle bond length (Å) for Mn(III)-alkylperoxo complexes (red ▲, adapted with permission from ref 19; Copyright 2013 American Chemical Society) and the $Mn(III)_2$ peroxo dimer **2** in this study (blue ●). Metrics for **2** are not included in the correlation.

The novelty of peroxo-bridged intermediate **2**, as well as the ability of the Mn(II) precursor complex to activate O_2 in a manner similar to examples found in nature (*vide supra*), has prompted us to investigate the electronic structures of compounds **1**−**3** in greater detail. The aforementioned correlation, and the associated unusually long Mn···pyridine distances in both binuclear $Mn(III)_2$ species (**2** and **3**), has led us to explore in particular the manner in which the pyridine ligands participate in bonding with the metal. While these locally high-spin $Mn(III)_2$ $(d^4)_2$ systems would possess a degenerate ground state in an octahedral ligand field, the significantly elongated bonds, as well as the heterogeneity of the ligating atoms, lead us to believe that this effect is not solely a manifestation of the predicted Jahn−Teller distortion. The significantly shorter $Mn-N_{py}$ bonds of the related, less sterically encumbered complex $\{[Mn^{III}(S^{Me2}N_4(6\text{-H-DPEN}))]_2(\mu\text{-}O)\}^{2+}$ support this conclusion.[18] Also of specific interest is the identification of the electronic and structural factors that may contribute to Mn-promoted O_2 activation.

In addition to mechanistic information, small-molecule bioinorganic chemistry provides a vital source of benchmark spectroscopic parameters essential for the identification of biological intermediates in the absence of an X-ray crystallographic structure.[20,21] In particular, spectroscopic methods with high chemical selectivity have proven indispensible for characterizing highly complex and short-lived enzymatic intermediates in systems such as PSII.[22] Often times, both theoretical and spectroscopic insight gained from small-molecule studies constitute an integral part of deciphering the spectroscopic data.[22−25] Many of these selective methods are at times complicated by factors such as polynuclearity and unfavorable selection rules, however, and thus a multitechnique approach often proves more successful. Furthermore, many of these methods yield information solely about the metal ion(s), such as oxidation state, spin state, and coordination environment. Identifying changes in ligand or substrate structure, e.g., dioxygen activation, are frequently of equal or greater interest.[15,23] To this end we have therefore investigated the series of Mn complexes described above (**1**−**3**) using a combined absorption and emission X-ray spectroscopic approach.

Transition metal K-edge X-ray absorption spectroscopy (XAS) has been widely utilized with great success for the study of metal sites in both biomolecules and small-molecule complexes.[23,26−30] The inherent element-specificity of transitions involving a 1s core electron makes it an ideal choice for the study of metalloenzymes, where the atom(s) of interest in the sample is often a mere fraction of a percent by mass. Additionally, the various regions of the XAS spectrum can yield information regarding coordination number and geometry, oxidation state, and metal−ligand distances.[31] For the vast majority of first-row transition metals, the lowest-energy absorption transitions in the pre-edge region correspond to Laporté-forbidden 1s to 3d excitations. The major contribution to intensity in this region involves the introduction of dipole character via the mixing of metal p character into the d manifold.[31] This p−d mixing depends greatly on metal ion geometry, coordination number, and ligand covalency. To higher energies lie the edge (1s to 4p transitions) and the continuum. The pre-edge and edge regions together are collectively known as the X-ray absorption near edge, or XANES region.

While XAS provides a wealth of information on the oxidation state and geometric environment of metal ions, it probes unoccupied orbitals, and is thus relatively insensitive to nonlocal changes in electronic structure. The study of the occupied valence orbitals however provides an excellent picture of both metal−ligand bonding as well as ligand, i.e., substrate, activation. These occupied metal and ligand orbitals can be interrogated in an element-specific fashion by measuring the X-ray fluorescence that can occur following photoionization of a core electron. Kβ X-ray emission spectroscopy (XES) has therefore been established as a probe of both metal and ligand properties.[32−35] In a one-electron approximation, the 1s core

DOI: 10.1021/acs.inorgchem.5b00699
Inorg. Chem. 2015, 54, 6410−6422

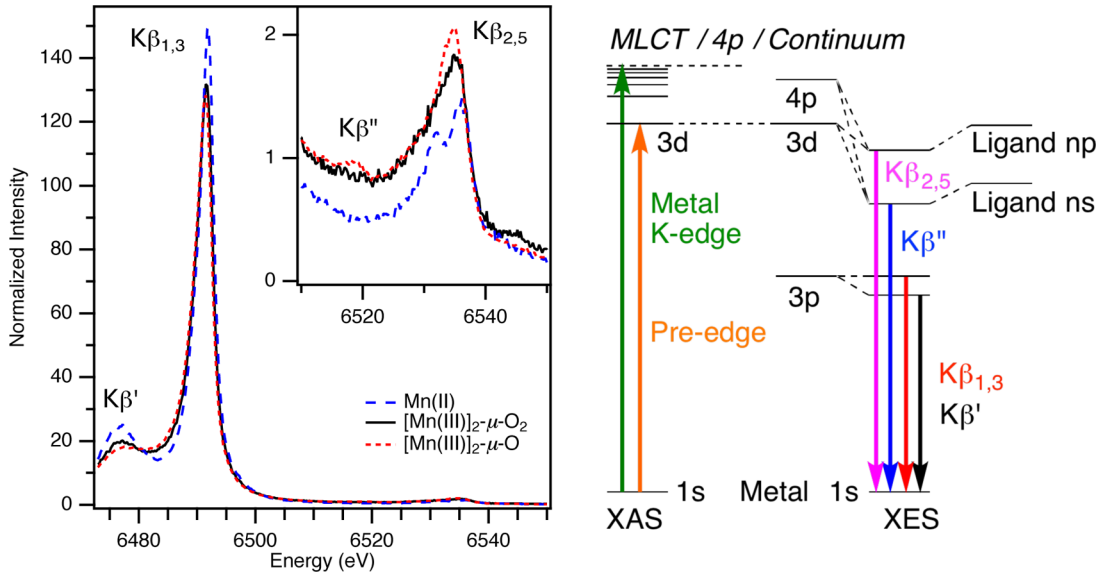

Figure 2. Left: Kβ XES spectrum of $[Mn^{II}(S^{Me2}N_4(6\text{-Me-DPEN}))](BPh4)$ (**1**) (dashed blue), $[Mn^{III}(S^{Me2}N_4(6\text{-Me-DPEN}))]_2(trans\text{-}\mu\text{-}1,2\text{-}O_2)(BPh_4)_2$ (**2**) (solid black), and $[Mn^{III}(S^{Me2}N_4(6\text{-Me-DPEN}))]_2(\mu\text{-}O)(BPh_4)_2$ (**3**) (dotted red). Inset: Enlarged VtC region. Right: Qualitative energy-level diagram of the absorption and emission processes discussed herein.

hole serves as the acceptor in transitions originating from a range of donor orbitals, which provides a wealth of information regarding electronic structure and bonding. The Kβ XES spectrum can be split into two regions: the lower energy and higher-intensity Kβ mainline, assigned as a dipole-allowed metal 3p to 1s emission, and the higher-energy and considerably less intense valence to core (VtC) region, corresponding to emission from occupied valence orbitals (Figure 2).[31,32] Due to the nature of their origins, the chemical information contained in these two features is quite complementary. The Kβ mainline provides insight into the local electronic structure of the metal, e.g., oxidation and spin state, while the VtC serves as a probe of the occupied valence orbitals involved in metal−ligand bonding.

The Kβ mainline, shown in Figure 2 for the compounds in this study, is split into two features: the higher-energy $Kβ_{1,3}$ and the lower energy Kβ′. This splitting has been attributed to exchange coupling of the unpaired 3p electron with unpaired electrons in the 3d shell, and thus is highly sensitive to the local spin state of the metal.[31,36] The inset of Figure 2 shows the VtC region, which is also composed of two distinct features: the higher-energy and higher-intensity $Kβ_{2,5}$ and the weaker, lower-energy Kβ″, which is only well-resolved in the case of **3**. As the name suggests, these features correspond to electronic transitions involving valence donor orbitals, which in the case of first-row metal complexes are typically the metal 3d and the ligand 2s/2p, or in the case of heavier ligands such as S the 3s/3p. The $Kβ_{2,5}$ is assigned as transitions originating from molecular orbitals with primarily ligand p character, while the Kβ″ is attributed to ligand s orbitals.[31,32] Similar to the absorption pre-edge, the intensity mechanism for these VtC transitions is largely dominated by mixing of metal p character into these valence orbitals, imparting transition dipole intensity. Both geometric effects and covalent ligand interactions contribute to metal p mixing. It has been previously shown that typically only σ-type ligand interactions give rise to appreciable VtC intensity, as they have the correct symmetry to mix with metal p orbitals.[31,37]

Density functional theory (DFT) calculations employing a simple one-electron model have proved to be quite successful in the quantitative calculation of the Kβ VtC region.[28,38,39] Assignment of key spectral features in the VtC to primarily ligand-based molecular orbitals using this DFT method has been shown to be highly effective in tracking changes to ligand structure throughout a series of complexes.[40] As with XES, analysis of the XAS using a DFT-based approach enhances the geometric and electronic structure information provided by this technique.[29,41] Unlike XES, however, these absorption processes generally require time-dependent DFT (TD-DFT) methods, and are at times less successful in their quantitative prediction of experimentally determined energies and intensities.[41,42] Transitions that are primarily metal-localized have been successfully reproduced using hybrid density functionals, but those that are charge transfer in nature are often poorly described.[42] Nevertheless, it is certainly instructive to obtain qualitative insight into these transitions, particularly when used in conjunction with a similar analysis of XES data.

In this study, we have used a combined XAS/XES/DFT-based approach to investigate a series of three recently reported Mn complexes (*vide supra*).[17,18] This system constitutes a rare example of a small-molecule Mn(II) complex performing well-characterized O_2 activation, and the isolation and crystallographic characterization of peroxo-bridged **2** presents a unique opportunity to obtain insight into both the mechanism of Mn-mediated O−O bond activation as well as the X-ray spectroscopic features associated with this moiety. The complementary and site-selective nature of XAS and XES, as well as the sensitivity of VtC XES to changes in ligand structure, highlights the applicability of these results to the study of Mn-containing biological systems involved in both the activation and formation of dioxygen.

EXPERIMENTAL SECTION

Synthesis and Sample Preparation. $[Mn^{II}(S^{Me2}N_4(6\text{-Me-DPEN}))](BPh_4)$ (**1**), $[Mn^{III}(S^{Me2}N_4(6\text{-Me-DPEN}))]_2(trans\text{-}\mu\text{-}1,2\text{-}O_2)(BPh_4)_2$ (**2**), and $[Mn^{III}(S^{Me2}N_4(6\text{-Me-DPEN}))]_2(\mu\text{-}O)(BPh_4)_2$ (**3**) were synthesized as previously reported.[17,18] Solution samples

DOI: 10.1021/acs.inorgchem.5b00699
Inorg. Chem. 2015, 54, 6410−6422

for absorption measurements were prepared as saturated solutions of crystalline solid in acetonitrile (**1** and **3**) or propionitrile (**2**) at 10−15 mM. Solutions were loaded into 1 mm cells with a 38 μm Kapton tape window and immediately frozen in liquid N_2. Solid samples for emission measurements were prepared by diluting crystalline solid of **1**, **2**, and **3** with boron nitride (approximately 1:1 by mass). The mixture was ground into a homogeneous powder with a mortar and pestle, sealed in Al spacers with Kapton tape, and frozen in liquid N_2. Due to the thermal instability of **2**, samples of this compound were prepared at 195 K in a freezer or on a bed of dry ice. To prevent condensation of water, solid samples were prepared under a blanket of Ar.

XAS and XES Measurements. Data were collected at the European Synchrotron Radiation Facility (ESRF) beamline ID-26, equipped with a Si(111) double crystal monochromator, and a LHe cryostat (10 K) sample chamber. Kβ X-ray emission spectra were measured at an incident energy of 6700 eV using five Si(440) crystal analyzers and an avalanche photodiode detector (APD) in a Rowland geometry, as previously described.[34] X-ray absorption data were measured in both total fluorescence yield (TFY) and Kβ detection modes using discrete photodiodes. Kβ detected XAS were measured by holding the angle for the analyzer crystals fixed to the maximum energy of the Mn K$\beta_{1,3}$ emission line for each respective compound. The incident flux at the sample was $\sim 10^{13}$ photons/second in a 0.2 × 1.5 mm^2 beam spot. In order to assess radiation damage and determine the acceptable dwell time per sample spot, short (5−6 s) Kβ-detected XANES scans were measured to assess the rate of photoreduction. If necessary, aluminum foils were inserted into the beam path to attenuate the incident flux. Only scans that showed no evidence of radiation damage were included in the final analysis. Acceptable scans were averaged using PyMCA.[43]

Analysis of XAS Spectra. Mn K-edge XAS spectra of $KMnO_4$ were used as an energy calibration reference, with the pre-edge maximum at 6543.3 eV.[42] For all XAS data, a linear pre-edge function and a quadratic polynomial for the postedge were used for background subtraction, followed by normalization of the edge jump to 1. In order to extract intensities and energy positions, the pre-edges were fit with pseudo-Voigt functions, and a cumulative pseudo-Voigt function was used to model the edge jump. The intensity of the features corresponds to the integrated area under the peaks. The software package PeakFit v. 4.12 was used for the fitting.

Analysis of XES Spectra. The mainline regions of all spectra were modeled with a sum of 4 pseudo-Voigt functions and fit using MATLAB. The VtC region of **1** was then modeled using a sum of 5 pseudo-Voigt functions to identify contributions from the N and S atoms of the ligand. These functions were used as a starting point to model the VtC regions of **2** and **3**, where the peak positions and intensities were allowed to float but the fwhm and Lorentzian fraction were held fixed to within 5%. For initial modeling of **2** and **3** the region between 6512 and 6522 eV, corresponding to the Kβ'' observed in **3**, was excluded and the remainder of the VtC region fit using the functions present in **1**. An additional function was then added to describe the O contribution in the Kβ'', and a fit of solely that function performed for **2** and **3**. Finally, all constraints were removed, and fits of the full XES spectra were performed. The intensities of the final fits were then used to normalize the total integrated XES spectral areas to 1000. It should be noted that fits for **2** and **3** using two functions instead of one to model the O contribution produced solutions with lower adjusted R^2 values. Due to intrinsic errors associated with this method of modeling the mainline background in the VtC region, we have previously estimated an error of ∼10% in our experimental VtC areas.[38] In the present case of highly related compounds, however, we expect error associated with the *relative* VtC area determinations within the series to be lower.

Computational Details. All calculations were performed using the ORCA v. 3.0 quantum chemistry package,[44] making use of the zeroth-order regular approximation for relativistic effects (ZORA),[45] the dispersion correction of Grimme and co-workers (D3BJ),[46,47] and the scalar-relativistically recontracted def2-TZVP(-f) basis set throughout.[48] A dense integration grid (Grid4) was employed, along with the fully decontracted def2-TZVP/J auxiliary basis set and the conductor-like screening model (COSMO) using dichloromethane as the solvent (ε = 9.08).[49] Geometry optimizations and analytical frequency calculations were initiated from X-ray crystallographic coordinates using the BP86 functional[50,51] with the resolution of the identity (RI) approximation.[52] VtC XES calculations were performed within a one-electron DFT model, and were corrected for spin−orbit coupling using the spin−orbit mean-field method[53] as described previously.[33,34,38] XAS calculations were performed using the B3LYP functional and the TD-DFT method employing the Tamm−Dancoff[54,55] and the RI chain of spheres (RIJCOSX) approximations.[56−58] Fragment analysis was performed with MOAnalyzer,[59] and transition difference densities for XAS calculations and canonical orbitals for electronic structure and XES calculations were visualized with UCSF Chimera.[60] Normal mode trajectories were animated and visualized using Avogadro.

RESULTS AND DISCUSSION

Experimental K-Edge XAS Data. Comparison of the XAS data collected in both total fluorescence yield (TFY) and at the Kβ mainline revealed improved resolution of the pre-edge spectral features for the latter method. The Kβ detected absorption, also known as Kβ high-energy resolution fluorescence detected absorption (Kβ HERFD absorption), is expected to mitigate spectral broadening due to finite core-hole lifetimes.[31,61,62] While detection at the K$\beta_{1,3}$ line should theoretically select preferentially for excitations of the β spin core electrons, quantitative comparison of the TFY and Kβ HERFD XANES spectra reveals no significant changes aside from a sharpening of the pre-edge features (see Supporting Information). This suggests that either there is sufficient multiplet structure in the mainline within the resolution of the spectrometer to negate this effect or that the contributions of α spin excitations are negligible.[31] While the latter is certainly true in the case of **1** given the high-spin d^5 configuration, it is likely that a combination of both effects contributes to the absence of significant differences in the intensity trends of the TFY and HERFD data. Due to the improved resolution we have elected to proceed with our analysis using the HERFD XAS data, and acknowledge that when compared to our TD-DFT calculations, the physical representation is not strictly accurate. The TFY spectra, as well as a table of fits of the data, are provided in the Supporting Information for comparison (Figures S-1−S-3 and Table S-1).

Normalized Kβ HERFD XAS spectra for **1**−**3** are shown in Figure 3. The energy of the rising edge is found to increase by ∼2.1 eV upon conversion of **1** to peroxo **2**, indicating a one-electron oxidation of the Mn (Table 1). The identical rising edge energy of **3** is again consistent with an increase in oxidation state relative to **1**. Preceding the rising edge, all complexes exhibit a pre-edge consisting of two well-resolved features at ∼6540 and ∼6542.5 eV (Figure 3, bottom). For Mn complexes with extended π systems, the low and higher-energy pre-edge features have previously been assigned as 1s to 3d and metal-to-ligand charge transfer (MLCT) transitions, respectively.[42]

Comparison of the first pre-edge feature for Mn(II) **1** and peroxo **2** reveals a distinct decrease in intensity in **2** despite the increase in oxidation state. As X-ray absorption intensities are dominated by dipole character, a decrease in intensity of the 1s to 3d feature is consistent with a decrease of p mixing into the 3d manifold, which is often governed by the symmetry at the metal center. The distorted trigonal bipyramidal geometry of **1** (τ = 0.59) should allow for more efficient p−d mixing than in

DOI: 10.1021/acs.inorgchem.5b00699
Inorg. Chem. 2015, 54, 6410−6422

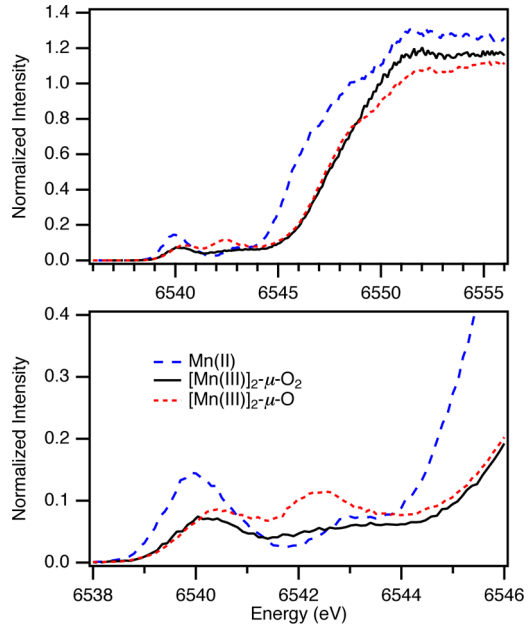

Figure 3. Top: Kβ HERFD XANES for compounds **1**−**3**. Bottom: Expansion of the pre-edge region.

six-coordinate **2** or **3**. A marked increase in the area of the second pre-edge (MLCT) feature in **3** is observed upon comparison of the two $Mn(III)_2$ compounds **2** and **3**. Inspection of the X-ray crystal structures of these compounds reveals that upon conversion of **2** to **3** the weakly coordinated pyridine ligands elongate further (mean distance of 2.451−2.541 Å), which should serve to decrease the intensity of charge transfer transitions into the pyridine π^* framework. The opposite change observed in the data could be explained by MLCT acceptor orbitals of a different nature, or by some mechanism for increasing the transition dipole moment integral along the Mn-pyridine vector. To further understand the observed trends, as well as the properties of these transitions, time-dependent DFT calculations were carried out for all compounds (*vide infra*).

Experimental Kβ XES Mainline Data. The profile of Kβ mainlines is highly dependent on the 3p−3d exchange coupling, modulated by total spin and covalency of the metal center. The Kβ mainline of **1** (Figure 4) is consistent with a high-spin Mn(II) complex, having a K$\beta_{1,3}$ energy of ∼6491 eV and a well-resolved Kβ' feature. Upon oxidation to Mn(III) a shift of the K$\beta_{1,3}$ to lower energy for complexes **2** and **3** is observed, as well as a decrease in the Kβ' intensity. This was previously described as being due to the decrease in spin at the metal from $S = {}^5/_2$ to $S = 2$, resulting in a diminished p−d exchange integral, which causes a decrease in the Kβ'−K$\beta_{1,3}$ splitting (ΔE_{main}) and a lowering of the K$\beta_{1,3}$ energy.[63] A

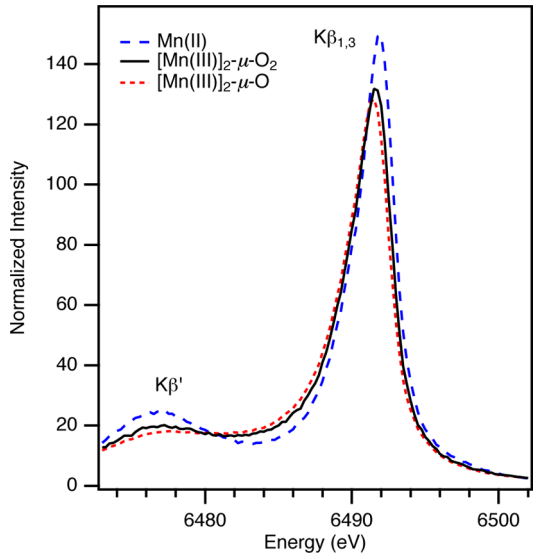

Figure 4. Kβ mainlines of **1**−**3**.

further contraction in the ΔE_{main} is observed upon conversion of **2** to **3** (Table 2). As both **2** and **3** have two high-spin

Table 2. K$\beta_{1,3}$ and Kβ' Energies and Corresponding ΔE_{main}

	K$\beta_{1,3}$ (eV)	Kβ' (eV)	ΔE_{main} (eV)
Mn(II) **1**	6492.0	6477.2	14.8
peroxo **2**	6491.6	6477.2	14.4
oxo **3**	6491.4	6477.6	13.8

Mn(III) ions as previously reported and further evidenced by XAS analysis, the modest difference in the Kβ'−K$\beta_{1,3}$ splitting can be attributed to increased Mn−O covalency in **3**.[36]

Experimental Kβ XES Valence-to-Core Data. The higher-energy VtC region provides complementary information on the properties of the primarily ligand-based valence molecular orbitals. Experimental data and fits for the VtC regions are shown in Figure 5, and the corresponding energies and experimental and calculated VtC areas are reported in Table 3.

Comparison of the K$\beta_{2,5}$ Regions. The K$\beta_{2,5}$ region of **1** is composed of two well-resolved peaks (Figure 5 top), in significant contrast to the spectra of **2** and **3**. Features in this spectral region typically arise from the highest-energy occupied ligand valence orbitals, which in the case of these compounds are the nitrogen and oxygen 2p and sulfur 3p orbitals. The presence of two distinct peaks in **1** suggests two sets of donor orbitals with significantly different ionization potentials.[37] Valence-to-core transitions gain intensity through introduction of metal p character into the donor orbitals, so generally transitions with observable intensity correspond to donor

Table 1. Experimental (HERFD) and Calculated Mn K-Edge XAS Parameters

		expt pre-edge 1 (1s to 3d)		calcd pre-edge (1s to 3d)[a,b]		expt pre-edge 2 (MLCT)	
	rising edge energy (eV)	energy (eV)	intensity (×10^2)	IWEA (eV)	intensity (×10^6)	energy (eV)	intensity (×10^2)
Mn(II) **1**	6545.5	6540.1	20	6507.5	56.3	6543.1	9
peroxo **2**	6547.6	6540.3	9	6508.2	52.0	6543.0	11
oxo **3**	6547.6	6540.4	10	6508.2	34.7	6542.4	17

[a]IWEA: intensity weighted energy average. Procedures for obtaining the IWAE and calculated intensities are described in ref 42. [b]Calculated intensities for **2** and **3** are divided by 2 to normalize to the number of Mn ions.

DOI: 10.1021/acs.inorgchem.5b00699
Inorg. Chem. 2015, 54, 6410−6422

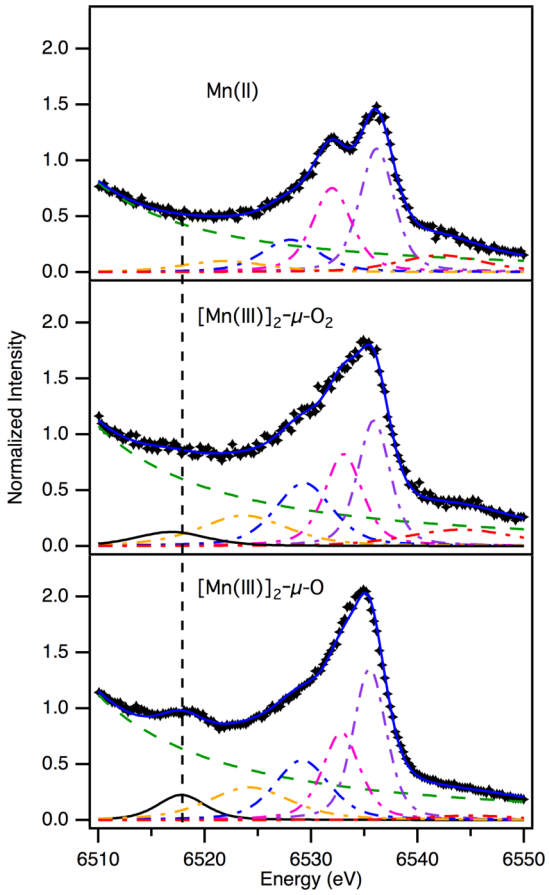

Figure 5. Experimental data (black points) and fits of the VtC regions of **1**−**3**. The blue solid trace represents the total fit, the green dashed trace is the Kβ mainline background, and the black solid peak represents the fit component attributed to O 2s contributions. Vertical dashed black line is a visual guide, centered on the maximum of the black fit component in oxo-bridged **3** at 6517.8 eV, showing a blue-shift of the O contributions in **3** relative to peroxo-bridged **2**, and the lack of significant Kβ'' in Mn(II) **1**.

Table 3. Kβ'' Energies and K$\beta_{2,5}$ IWAEs, Experimentally-Determined Valence-to-Core Areas, and Calculated Valence-to-Core Areas[a]

	Kβ'' (eV)	K$\beta_{2,5}$ IWAE (eV)	expt area	calcd area[a]
Mn(II) **1**		6534.3	12.7	15.0
peroxo **2**	6516.8	6534.5	18.7	20.5
oxo **3**	6517.9	6534.4	19.5	21.8

[a]Calculated VtC areas were obtained by summing over all calculated oscillator strengths in the spectral window from the combined electric and magnetic dipole and electric quadrupole transition moments and multiplying by 1000.

orbitals that interact with the metal in a σ-fashion. The distorted 5-coordinate geometry of **1** however is expected to significantly mix the pseudotrigonal plane (*vide supra*), resulting in intensity not only from ligand orbitals but also potentially Mn d orbitals as well.[63] The presence of two peaks of different energies in the K$\beta_{2,5}$ feature of **1** could therefore be rationalized as higher-energy transitions being mostly Mn d in nature and lower-energy transitions originating from imine and pyridine π or sulfur p orbitals.

Additionally, there is a marked increase in the experimental areas of the VtC for **2** and **3** compared to **1** (Table 3). The increase in oxidation state should lead to an increase in VtC intensity via contraction of most of the metal−ligand bonds, and coordination of a sixth (per)oxo ligand should also increase the number of transitions.

Comparison of the Kβ'' Regions. The more clearly assignable features of the peroxo- and oxo-based orbitals are found in the Kβ'' region, and correspond to orbitals which are oxygen 2s in character.[34] This is most clearly observed in the Kβ'' region of **3**, where the black fit component centered at ∼6518 eV has been assigned as VtC emission originating from an oxo 2s orbital (Figure 5). Comparison of the same fit component for **2** reveals distinct changes indicative of a change in the coordinated species. The Kβ'' feature is shifted to lower energy by ∼1 eV (Table 3), and has only 84% of the intensity of **3**. The full width at half max (fwhm) of the black fit component is also increased to 150% of that of **3**. These changes are all consistent with the assignment of the black fit component in **2** as representative of transitions originating from peroxo 2s orbitals. The peroxo ligand is expected to have VtC transitions arising from both 2s−2s bonding and 2s−2s antibonding combinations.[40] Though not resolved in this spectral region, the significant increase in the fwhm is consistent with discrete transitions at different energies in place of a single transition expected in **3**. Furthermore, the decreased intensity can be attributed to the longer (by 0.072 Å) Mn−O bonds in **2** versus **3**. The lack of any significant deviation from the Kβ mainline tail (green dashed trace, Figure 5) below ∼6518 eV (vertical line) for **1** is consistent with the absence of any oxygen ligands, while in the case of **2** and **3** this divergence begins at ∼6511 eV. This illustrates the the ability of the VtC XES technique to accurately distinguish the identity of light-atom ligands, and supports the presence of an additional fit component in this region for **2**.[30,32]

Density Functional Theory Calculations. To further understand the electronic structure and XAS/XES spectra of the complexes examined herein, DFT calculations were performed. In all cases, the optimized geometries were found to be in good agreement with the crystallographically determined structures, with an average deviation in first-coordination sphere metrics of 0.0206 Å (detailed comparison available in Supporting Information Figure S-10). Importantly, the average deviation of the Mn···N_{py} distances in **2** and **3** is only 0.030 Å, suggesting that the effects responsible for these unusually long distances observed in the crystal structures are successfully represented in the calculations. The distorted trigonal-bipyramidal geometry of **1** and the ^{6}S ground state at the Mn(II) free ion limit lead to a substantially hybridized d manifold, making definitive assignment and ordering challenging.

The d manifold of the peroxo **2** is somewhat better defined, and inspection of both the orbital contributions and the isosurface plots provides considerable insight into the electronic structure of this novel complex. As shown in Figure 6, the molecular *z*-axis is oriented along the Mn-pyridine vector, with the unoccupied $d_{x^2-y^2}$ pointed at both the sulfur and peroxo ligands. In the α spin manifold the singly occupied d_{z^2} thus points at the pyridine nitrogens, and is σ-antibonding with the nitrogen lone pairs. This highly unfavorable interaction is likely the rationale for both the long Mn−pyridine distances as well as the correlation shown in Figure 1. The Mn d_{xy} orbital is also worth mentioning, as this formally Mn−ligand antibonding combination is shown to in fact have a π-type bonding interaction with the in-plane peroxo π^*. In the β spin manifold

DOI: 10.1021/acs.inorgchem.5b00699
Inorg. Chem. 2015, 54, 6410−6422

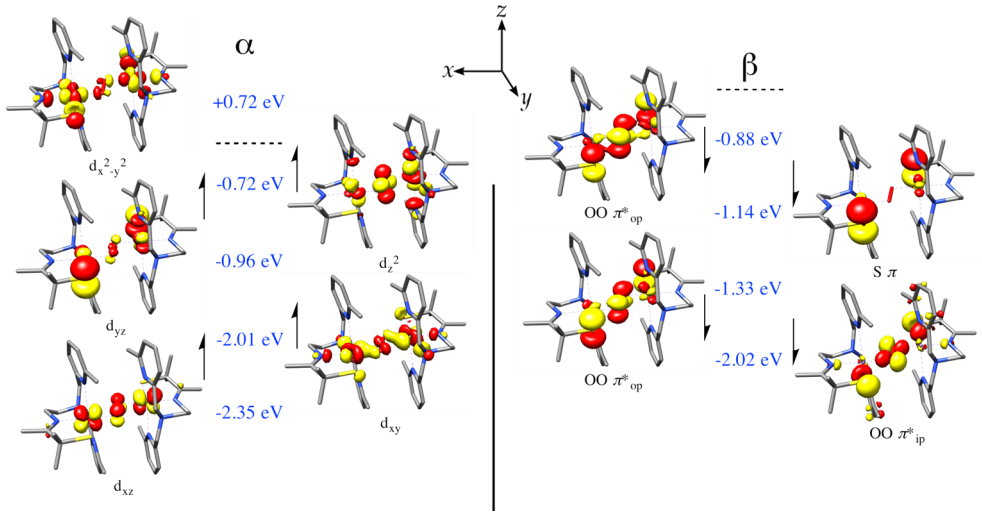

Figure 6. Molecular orbital diagram for peroxo-bridged **2**, showing the orientation and ordering of the d manifold, orbital energies and occupancies, and relevant metal−ligand interactions. The dashed line represents the Fermi level, set to 0 eV as the halfway point between the calculated HOMO and LUMO energies. Canonical molecular orbital surfaces are shown at an isovalue of 0.05.

the three highest-lying molecular orbitals are combinations of sulfur p and out-of-plane peroxo π^*. As can be seen from the isosurface plots, there is Mn character in these orbitals, despite the fact that they are formally occupied peroxo orbitals and the Mn ions are d^0 in the β spin manifold. This delocalization of peroxo O−O antibonding electron density onto the Mn likely helps to stabilize this intermediate species. Finally, the lowest-energy β orbital shown is the in-plane peroxo π^*, which, like the α-spin LUMO, also has correct symmetry to mix with the σ-interacting sulfur $3p_y$. The electronic structure for **3** was found to be similar, with an identical orientation of the d manifold and less mixed Mn orbitals as a result of the loss of the high-energy peroxo antibonding orbitals. Additionally, a single-point calculation performed on **3** utilizing the B3LYP functional and the broken-symmetry formalism for magnetic coupling[64] correctly predicted the sign and magnitude of the coupling constant $J = -126$ cm^{-1} (experimentally determined: $J = -125.6$ cm^{-1}).[18] The implications of these results relating to possible mechanisms of O−O bond activation will be discussed following comparison of calculated XAS and XES spectra to experimental results.

Calculated K Pre-Edge XAS. In all cases the calculated pre-edge spectra (Figure 7) are found to have two distinct features: a low-energy peak arising from transitions to Mn 3d orbitals and a higher-energy peak found to be mostly due to MLCT transitions. A 32.6 eV shift was applied to all calculated spectra in order to align theory with experiment,[42] and for **3** the low-spin broken symmetry solution was utilized.

In the case of **1** the 1s to 3d pre-edge feature consists of transitions to five d orbitals acting as acceptors for 1s β-spin excitations. The distorted trigonal-bipyramidal geometry at the metal center greatly favors p−d mixing, and the calculated % Mn p character in the pre-edge for **1** (~6% p) is thus significantly higher than in **2** and **3** (~1.7% p). The MLCT peak in **1** predominantly consists of transitions from the Mn 1s to the π^* of the pyridine ligands, which is also indicative of substantial p−d mixing within the trigonal plane. For **2** and **3** the lowest-energy calculated pre-edge feature also consists of 1s to 3d transitions, as evidenced by the difference density surfaces in Figure 7. In both cases the calculated 1s to 3d transitions show roughly the same percentage of p character, and are

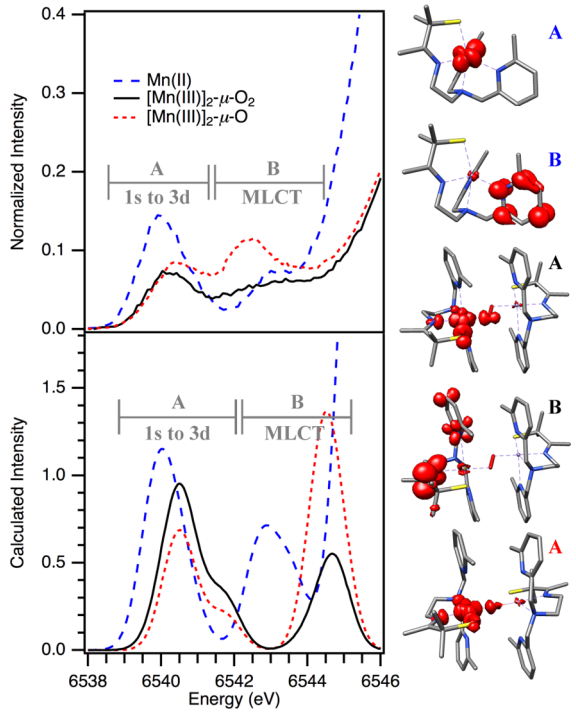

Figure 7. Experimental (top) and calculated (bottom, 1 eV broadening) pre-edge spectra. Spectra for peroxo **2** and oxo **3** are divided by 2 to normalize to the number of Mn ions. Region A is assigned as 1s to 3d excitation and region B is MLCT. Representative TD-DFT transition difference densities are shown at an isovalue of 0.005, and correspond to compound and transition type by label color. MLCT transitions for oxo **3** were found to be very similar to those of peroxo **2**.

dominated by excitations into the empty $d_{x^2-y^2}$. The K$\beta_{1,3}$ HERFD detection method filters out transitions with higher multiplicities (*vide supra*). In a rough approximation the transitions in the α spin manifold, which are fully weighted in the TD-DFT-calculated spectra, are suppressed in the experimental data. The total pre-edge transition intensity in the calculated spectra of the Mn(III)$_2$ complexes **2** and **3** is therefore larger than the experimental spectra, as a single α spin

DOI: 10.1021/acs.inorgchem.5b00699
Inorg. Chem. 2015, 54, 6410−6422

transition is expected in the high-spin d^4 configuration. The pseudo-octahedral geometry of these compounds should disfavor geometric p−d mixing mechanisms, and instead, metal p character is introduced via covalent bonding with both the sulfur and oxygen ligands, as also seen in the displayed transition difference densities. Coordination of the pyridine ligands despite their long metal−ligand distances is substantiated by MLCT transitions to the pyridine ligands found in both **2** and **3**. In addition, MLCT transitions to the peroxo bridge in **2** and the oxo bridge in **3** are also present. The total % Mn p character in the calculated MLCT feature in **3** is slightly higher than in that of **2**, consistent with a more intense transition and a more covalent metal−ligand interaction. Given the strong electronic coupling of the two Mn(III) ions in oxo-bridged **3**, the peak at ∼6542.5 in the experimental spectrum could be a metal-to-metal charge transfer excitation. Transitions of this nature are known to be a shortcoming of the TD-DFT method, and this would rationalize the absence of this feature in our calculated spectrum.[65]

Calculated Valence-to-Core Spectra. To gain additional insight into the spectral features of the VtC region, theoretical spectra were calculated on the basis of the results of the DFT calculations similar to published procedures.[34] In order to visually compare the calculated VtC spectra with experimental results, the tails of the mainline fits (Figure 5, dashed green traces) were subtracted from the total fits of the XES spectra. These background-subtracted fits and the calculated VtC spectra are shown in Figure 8.

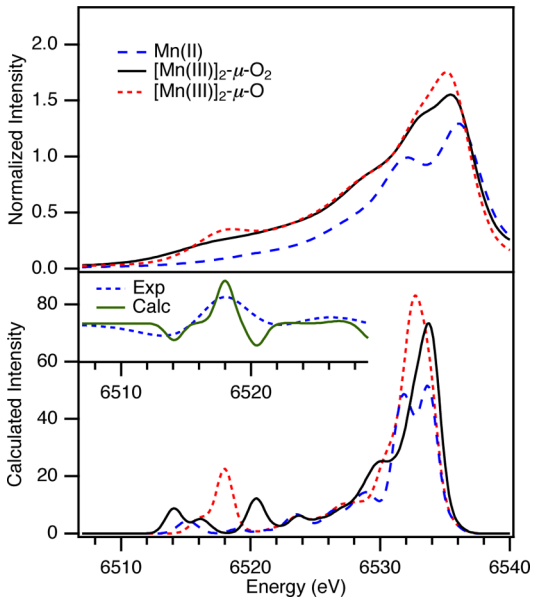

Figure 8. Top: Kβ-mainline-subtracted fits of experimental VtC regions. Bottom: Calculated VtC spectra (1.5 eV fwhm broadening). Inset: Difference of oxo-bridged **3** and peroxo **2**.

Several key features of the experimental fits are faithfully reproduced in the calculated spectra. In the Kβ″ region the presence of a pronounced peak in oxo-bridged **3** at 6518 eV and two lower intensity features in peroxo-bridged **2** are consistent with the experimental data, as well as the lack of significant Kβ″ intensity in **1**. The inset highlights the differences in the experimental Kβ″ regions between **3** and **2**, which are accurately predicted in the calculated spectra. The two Kβ″ features at ∼6514 and ∼6520.5 eV in the calculated spectrum of **2** are expected to arise from the peroxo 2s−2s bonding and antibonding combinations, respectively, and are consistent with a splitting of ∼7 eV observed by X-ray photoelectron spectroscopy.[66] As previously discussed, the increase in the fwhm of the corresponding fit component for **2** is also consistent with this assignment; however, there is not sufficient resolution from the mainline tail to permit quantitative determination of this splitting in the experimental data. The splitting of the $K\beta_{2,5}$ peak of **1**, however, is both experimentally resolved and well-reproduced in the calculated spectrum. Comparison of the calculated $K\beta_{2,5}$ features also shows **2** as having the highest-energy peak and **3** the most intense peak, both of which are consistent with the values reported in Table 3. Lastly, there is a strong correlation between the experimental and calculated VtC areas, the former obtained from integrated intensity of the VtC fits, both including and excluding the Kβ″ region (Supporting Information Figure S-11).

Spectral and Mechanistic Insight from DFT Calculations. The successful calculation of the experimental VtC spectral features, as well as the relative integrated spectral intensities, suggests a good electronic structure description of both the energy and Mn p composition of the occupied valence orbitals. Additionally, the presence of two features, the first with roughly correct intensity, in each of the calculated XAS spectra indicates that the DFT virtual orbitals are likely also consistent with the true electronic structure. This is of particular interest given the unoccupied $d_{x^2-y^2}$ configuration in the Mn(III) complexes **2** and **3**. It has been previously shown that the unique *trans* bridging peroxo core in **2** possesses a highly activated O−O bond, and that this species decays via peroxo bond scission.[17] To further assess the integrity of the presented DFT calculations with regard to an accurate description of O−O bond activation, calculated vibrational frequencies for **2** were compared to those previously determined by resonance Raman spectroscopy. As shown in Table 4, the absolute energies of both the Mn−O and O−O stretching modes are consistent with experiment. Perhaps more importantly, the predicted shifts resulting from double ^{18}O substitution are in excellent agreement, indicating that the calculated force constants, and thus respective bond strengths, are correct.

Table 4. Comparison of Experimental and Calculated Vibrational Frequencies for Mn−O and O−O Stretching Modes of Peroxo 2[a]

stretch	expt (^{18}O) (cm^{-1})	calcd (^{18}O) (cm^{-1})	expt shift ($^{16}O-^{18}O$)	calcd shift ($^{16}O-^{18}O$)
Mn−O	611 (586)	608 (582)	25	26
O−O	819 (772)	806 (759)	47	47

[a]Experimental values were determined by resonance Raman spectroscopy in ref 17.

The calculation of consistent X-ray absorption and emission spectra and the accuracy of the predicted vibrational frequencies provide strong evidence for the fidelity of the electronic structure calculations. Insight into the structure and reactivity of these complexes, as well as notable features of the X-ray spectra, can therefore be obtained from the calculations with confidence that they accurately reflect the experimental findings.

Fragment Analysis and MO Contributions to Calculated VtC Spectra. To begin to construct a picture of individual

DOI: 10.1021/acs.inorgchem.5b00699
Inorg. Chem. 2015, 54, 6410−6422

ligand contributions to the VtC regions, the calculated spectra were broken down by contributions per ligand fragment. Contributions from the peroxo and oxo fragments in **2** and **3**, respectively, are of obvious specific interest, as well as the determination of sulfur-based intensity for all compounds. Additionally, in an effort to assess the involvement and degree of coordination of the pyridine ligands (*vide supra*), contributions from the N-heterocyclic nitrogens and the backbone imine and amine nitrogens were split into two fragments. An advantage of employing a one-electron approximation for calculation of the VtC XES spectra is that the transition donor orbitals are simply the canonical orbitals obtained from a single-point DFT calculation. As such, visualization of the significant contributions to intensity requires only the inspection of the correct Kohn–Sham orbital. Unfortunately, the density of donor orbitals in the K$\beta_{2,5}$ region makes distinguishing the individual orbital contributions extremely challenging; however, the Kβ'' region is typically composed of a smaller number of transitions.

The peaks in the Kβ'' region for **2** and **3** shown in Figure 9 are as expected primarily (per)oxo in character. As the Kβ'' region is reflective of ligand molecular orbitals composed of predominantly atomic s orbital character, these are expected to be the peroxo 2s–2s bonding and antibonding combinations and the oxo 2s atomic orbital, respectively. The shoulder present at ∼6515 eV in both spectra is from nitrogen 2s-based

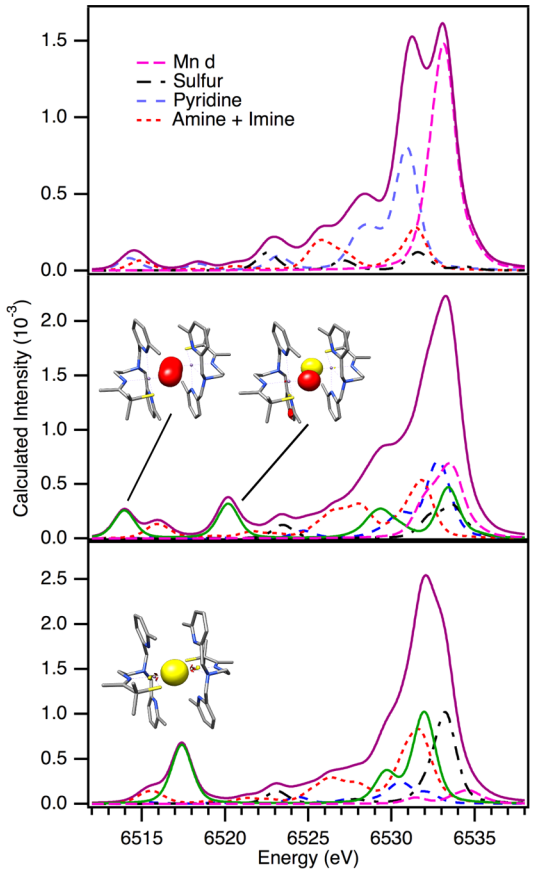

Figure 9. Fragment analysis of calculated VtC spectra based on donor molecular orbital contributions for Mn(II) **1** (top), peroxo-bridged **2** (middle), and oxo-bridged **3** (bottom). Canonical orbitals are shown at an isovalue of 0.05, and oxygen-based contributions are shown as a solid green trace.

orbitals originating from the backbone imine and amine nitrogens. Although this feature is not experimentally observable, it is worthwhile to note that in the case of **1** the nitrogen 2s peak in the Kβ'' is made up of contributions from both backbone and pyridine 2s orbitals. Given the strong distance dependence of VtC intensity, this is not altogether surprising, and additionally the increase in centrosymmetry of the new *z*-axis in **2** and **3** should reduce p–d mixing. Despite this there is still significant pyridine nitrogen p intensity in the K$\beta_{2,5}$ peak in **2** (Table 5), further supporting pyridine

Table 5. Percentage of Total Calculated VtC Intensity From Each Ligand Fragment

	Mn d	S	Pyr	Am + Im	total N	O
Mn(II) **1**	37%	7%	30%	15%	45%	
peroxo **2**	17%	9%	18%	23%	41%	22%
oxo **3**	4%	19%	8%	29%	37%	29%

involvement in coordination. As shown in Figure 9 and Table 5, however, the pyridine contribution to the total calculated VtC spectrum of **3** is significantly reduced relative to that of **2**, likely due to the further elongation of these bonds (by ∼0.09 Å). Conversion of the peroxo ligand in **2** to a more covalent, shorter oxo ligand in **3** forms a stronger σ^* interaction with the torus of the d_{z^2}, which seemingly results in an elongation along the molecular *z*-axis. The large amount of Mn d character in the VtC of **1** (Table 5) is attributed to significant p–d mixing due to the geometry. While it is somewhat uncommon to find such a large contribution from metal 3d orbitals, the result nicely parallels the findings from the analysis of the XAS pre-edge region (*vide supra*). The relatively large amount of Mn d character in **2** relative to **3** is rationalized by inspection of the isosurfaces in Figure 6, which show significant mixing of the peroxo π^* orbitals into both α and β d manifolds. The loss of these high-lying ligand orbitals in **3** should decrease this mixing and thus Mn d character. A similar effect explains the increase in sulfur contributions from peroxo **2** to oxo **3**, as the highest-lying ligand orbitals are now S 3p in character rather than peroxo π^*. Finally, the increase in oxygen character upon conversion of **2** to **3** is reflective of both increasing covalency and a shorter metal–ligand bond length.

Contributions to O–O Bond Activation. With an experimentally supported electronic structure description in hand, the factors affecting O–O bond activation were considered. The strong dependence of O–O bond length on the Mn–N-heterocyclic amine interaction can be explained by the σ^* orientation of the singly occupied d_{z^2} (*vide supra*), which results from the preferential orientation of the unoccupied $d_{x^2-y^2}$ toward both the stronger-field peroxo and thiolate ligands.[67] This interaction makes the Lewis acidity of the Mn highly sensitive to changes along this vector. The long Mn–N_{py} bonds in peroxo **2** should lead to a more Lewis acidic Mn(III) ion, and thus a stabilized peroxo O–O bond as previously shown.[19] Contraction of the Mn-pyridine distances, and thus decreasing Lewis acidity, should therefore lead to localization of more electron density in the peroxo π^* orbitals, weakening the peroxo bond and ultimately promoting O–O bond scission. A schematic for the mechanism of decreasing the Lewis acidity of the Mn ion is shown in Figure 10, and illustrates the contributing factors and the resultant localization of negative charge into peroxo antibonding orbitals. Given these interactions, a molecular vibration along the Mn-pyridine

DOI: 10.1021/acs.inorgchem.5b00699
Inorg. Chem. 2015, 54, 6410–6422

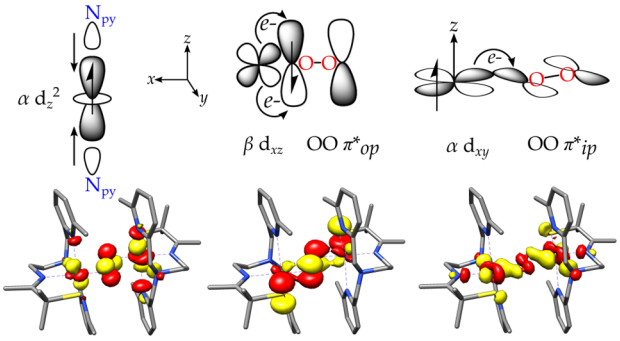

Figure 10. Schematic of the cause (left) and effect (middle, right) of decreased Mn Lewis acidity based on canonical spin-orbitals shown (from Figure 6). The peroxo π_{ip}* and π_{op}* are both π donors; however with decreasing Lewis acidity due to the N_{py} σ* interaction, electron density in Mn-peroxo π bonding MOs shifts off of the Mn ion and into the peroxo π* (as indicated by arrows), leading to an increase in O−O bond activation. Note that the center β-spin Mn d_{xz} spin-orbital is formally unoccupied; the population is due to delocalization of the occupied peroxo π_{op}* (*vide supra*).

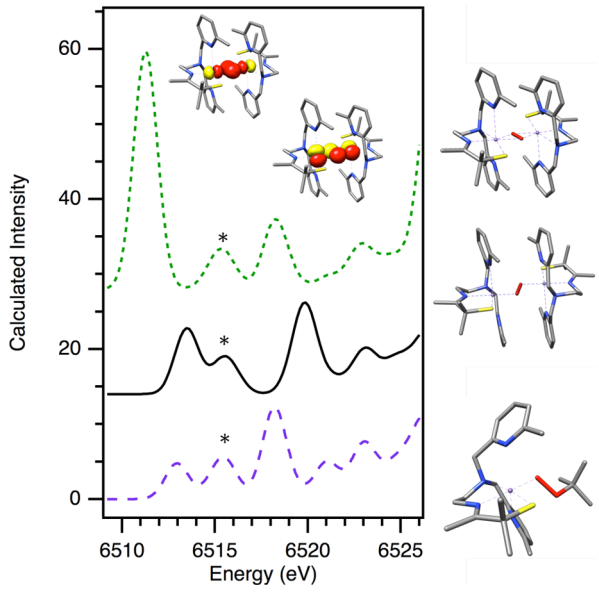

Figure 11. Calculated VtC Kβ'' spectra for side-on **2** (top, green dotted trace), **2** (middle, black solid trace), and $[(Mn^{III}(S^{Me2}$(6-Me-DPEN))(OOtBut)]$^+$ (bottom, purple dashed trace). Peaks marked with an * correspond to nitrogen 2s contributions from the ligand backbone, to lower energy are the 2s−2s bonding combinations, and to higher energy the antibonding combinations, as shown. Canonical orbitals are displayed at an isovalue of 0.05.

vector ultimately leading to O−O bond scission could be a possible mechanism for the decay of this intermediate. This is consistent with not only the thermal instability of **2**[17] but also the established correlations between O−O bond length (and thus Mn−N-heterocycle bond length) and the activation parameters $\Delta H^{\ddagger}$ and $\Delta S^{\ddagger}$.[19]

Spectroscopic Features of the Mn-Peroxo Unit. To our knowledge, this study represents the first application of XES to a Mn(III) peroxo complex of any kind. Given the novelty of the Mn(III)-peroxo dimer **2** in this work, as well as the importance of Mn peroxo moieties in catalytic function, some consideration was given to the spectroscopic parameters associated with this type of species. In particular, we considered the features of two key pieces of information for which XAS provides little insight: the identification of peroxo binding mode and the quantification of O−O bond activation. The large density of donor orbitals that comprise the K$\beta_{2,5}$ region makes the assignment of distinguishing features in this region difficult; however, the distinct energy of the peroxo 2s−2s combinations in the Kβ'' region, given sufficient resolution, are more amenable to systematic assignment.

Peroxo Binding Mode. Most Mn-peroxo compounds characterized to date have the peroxo unit coordinated in a side-on η^2 fashion;[68] therefore, investigation of the effect of coordination geometry on the relevant spectral features was of significant interest. VtC spectra were calculated for two additional structures using the same computational approach presented above. The first structure was generated by rotating the peroxo moiety of **2** such that it is entirely side-on relative to both Mn atoms. Bond lengths and angles of the Mn_2O_2 core were fixed, and the other coordinates were optimized. The second example is from the literature, and utilizes our previously reported "end-on" monomeric Mn(III) alkylperoxo ($[Mn^{III}(S^{Me2}$(6-Me-DPEN))(OOtBut)]$^+$, Mn−O−O = 112°).[19] As shown in Figure 11, all structures exhibit two peroxo features in the Kβ'' region: one to lower energy in the 6511−6513 eV range and one to higher energy around 6518−6520 eV. Similar to that of the peroxo dimer **2**, the lower energy feature can be assigned as the oxygen 2s−2s bonding combination while the higher-energy peak corresponds to the antibonding combination. As spectral intensity is governed by the mixing of Mn p character into these ligand orbitals, the coordination mode is shown to greatly influence the relative intensity of these two peaks. When the peroxo moiety is bound in a side-on fashion (Figure 11, top) the bonding combination expectedly has optimal overlap with the Mn 3pσ orbitals, while the antibonding combination is approximately orthogonal. Intensity in the antibonding combination was instead found to be due to the Mn 3pπ orbital, and the weaker π interaction expectedly results in diminished intensity. Isosurface plots of the bonding and antibonding combinations along with the relevant Mn 3p orbitals are also shown in Figure 11. As the optimized Mn−O−O bond angle is increased to 100° for the peroxo **2** and finally to 112° for the alkylperoxo, the ratio of bonding and antibonding intensity is found to change dramatically, as the 2s−2s bonding combination moves further from the Mn and the antibonding combination is increasingly oriented toward the Mn 3pσ. It is noted that investigation of a hypothetical end-on coordination mode was attempted in light of previous work on dinitrogen with a small-molecule iron complex (*vide infra*);[40] however, the sp hybridization of the oxygens required to accommodate this geometry is somewhat unrealistic and produced unsatisfactory results. The coordination mode of the peroxo unit in **2** thus has suboptimal orientation to provide appreciable Kβ'' intensity, and is likely the reason for the poor experimental resolution of this feature. These results suggest that the relative intensities in this spectral region may in future be used to determine the binding mode of Mn peroxo adducts.

Quantifying O−O Bond Activation. As previously mentioned, the vast majority of reported small-molecule Mn peroxo complexes have the peroxo unit bound in an η^2 side-on fashion. This binding mode is expected to result in significant Kβ'' intensity from the 2s−2s bonding orbital (Figure 11), and an accurate experimental determination of the energy of this feature should therefore be possible. Determining the degree of

DOI: 10.1021/acs.inorgchem.5b00699
Inorg. Chem. 2015, 54, 6410−6422

O−O bond activation based on this spectral feature would be an immensely powerful tool to investigate O_2 activation processes in both industrial and biological catalysis. We have therefore calculated the spectral changes expected to occur upon systematic variation of the O−O bond length. For this study, we have employed the Mn(III) 14-TMC-O_2 complex reported by Nam and co-workers,[69] and performed a relaxed surface scan, varying the O−O bond length and calculating a VtC XES spectrum at each geometry, again employing our prior computational approach (*vide supra*).

Figure 12 shows the results of these calculations, and a marked change in the energy of the peak due to the 2s−2s

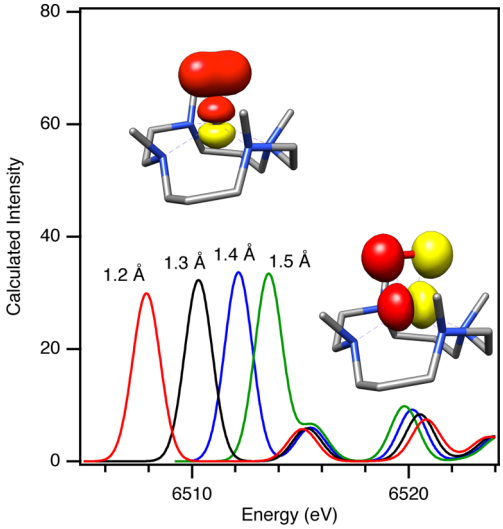

Figure 12. Calculated VtC Kβ'' spectra for $[Mn^{III}(14\text{-TMC})(O_2)]^+$ (ref 69) for varying O−O bond length. Canonical orbitals giving rise to spectral intensity (peroxo 2s−2s combinations and Mn 3pσ or π) are shown at an isovalue of 0.05.

bonding combination is evident, along with a negligible change in the energy of the antibonding combination. The destabilization of the bonding orbital upon elongation of the O−O bond is predicted from basic molecular orbital theory; however, the calculated change in energy, approximately 2 eV per 0.1 Å, is quite substantial. With the high experimental accuracy of modern solid-angle X-ray fluorescence spectrometers, in the linear approximation of this trend determining changes in O−O bond length of even 0.01 Å, corresponding to 0.2 eV, should be possible. We note however that, in light of the previous section, an orientation that promotes significant intensity of this feature is required. It is known from both previous studies on higher-valent Mn oxo complexes,[33] as well as from our characterization of oxo-bridged **3**, that, in the limit of a fully cleaved O−O bond, Kβ'' spectral features *are* observed which have been shown to be atomic oxygen 2s in origin. As shown in Figure 8, these transitions occur to higher energy of the peroxo bonding combination and to lower energy of the antibonding combination. Furthermore, an oxo ligand fragment will possess only the spherically symmetric atomic 2s donor orbital, rather than orientation-dependent bonding and antibonding combinations; therefore, spectral intensity is expected regardless of the coordination mode. This should allow for spectroscopic insight into not only the degree of activation of O_2 or reduced O_2 ligands but also the identification of a change in speciation upon cleavage of the O−O bond.

Generalization to the Study of Small-Molecule Activation. For chemical systems where high-resolution structural data are not available, assessing small-molecule activation in a quantitative and site-selective fashion is integral to advancing mechanistic understanding. VtC XES offers unique capabilities in this regard, as demonstrated both in the present work and in a recent investigation of dinitrogen activation by a small-molecule Fe complex.[40] A brief comparison of these two studies reveals some key similarities and differences that we believe help to define both the potential and the limitations of VtC XES in this application. Perhaps most important are the factors contributing to intensity, which are governed by mixing of metal p character into the ligand valence orbitals. The 3p shell of Mn is expected to be more diffuse than for Fe based on Slater's rules, which should lead to increased relative VtC intensity for Mn compounds of identical oxidation state, consistent with previous studies.[34,37,38] As we have shown in this work, however, the coordination mode of a diatomic small-molecule substrate is also of great importance for determining which of the 2s−2s combinations will dominate the Kβ'' intensity (*vide supra*). In this regard the end-on coordination mode found in the Fe N_2 study is expected to produce more favorable results. Not only is the dominant antibonding combination more diffuse, and thus more likely to mix with the metal p orbitals, but it also occurs to higher energy and is therefore expected to be better resolved from the tail of the Kβ mainline. Finally, it has recently been demonstrated that the angle of a light-atom ligand with respect to the orientation of the metal p manifold plays a role in governing VtC intensity, and in a simple Walsh diagram picture, σ-type ligand orbitals which bisect the Cartesian axes of the metal should provide maximum metal p mixing.[70] The observation of appreciable VtC intensity is dependent on favorable conditions with regard to at least some of these considerations.

SUMMARY AND CONCLUSIONS

This work presents the first XES study of a Mn-peroxo compound, and provides further electronic and structural insight into the only reported binuclear Mn(III)-peroxo complex to date. As such, it establishes essential spectroscopic benchmarks for analogous studies on less well-characterized systems. Furthermore, it is one of few examples of a combined XAS/XES study, and highlights the complementary nature of the information provided with regard to metal and ligand electronic structure. With the aid of DFT calculations, we have identified the origins of spectral intensity in both absorption and emission spectra, and shown how p−d mixing can be affected by both geometric effects and by highly covalent metal−ligand interactions. Correlations between experimental and calculated spectra have provided validation for our electronic structure description, and permitted assignment of observed spectral features to specific ligands and orbitals.

Analysis of the calculated electronic structure has allowed for the determination of both the ordering and the orientation of the Mn d manifold peroxo-bridged **2**. This insight has been used to answer questions regarding the degree of ligation of the pyridine ligand(s) in **2** and **3**, and to rationalize these exceptionally long metal−ligand bonds. It has also allowed us to propose a mechanism for O−O bond activation in this system involving both covalent charge donation by the thiolate sulfur as well as modulation of the Mn Lewis acidity via a strong

DOI: 10.1021/acs.inorgchem.5b00699
Inorg. Chem. 2015, 54, 6410−6422

σ^* Mn−pyridine interaction. The specific orbitals that may contribute to this process have also been identified, and these results suggest that synthetic adjustments may be possible to either further promote or disfavor O_2 activation. Current studies toward this goal are underway in our research groups.

Finally, comparison to a previous Kβ VtC XES study of dinitrogen activation has also illustrated some of the factors that may determine the success of this technique in future applications to small-molecule activation. Theoretical investigations based on reported compounds suggest that, given the proper metal and ligand geometry, this method may provide insight into not only changes in speciation but also determination of both the coordination mode and bond length of small-molecule substrates. The elemental selectivity of VtC XES, its quantitative nature, and novel information content serve to further highlight its potential application to small-molecule activation processes in both catalysis and bioinorganic chemistry.

■ ASSOCIATED CONTENT

Supporting Information

XAS spectra and fits of all compounds collected in TFY and HERFD modes, and tabulated spectral parameters based on TFY fits. Fits of Kβ XES mainlines used for background subtraction of the VtC regions for all compounds. Graphical correlation between experimental and calculated VtC areas, and comparison of metrical parameters obtained from geometry optimizations with the published crystallographic values. Sample input files used for geometry optimizations and spectral calculations, and optimized coordinates for all compounds. The Supporting Information is available free of charge on the ACS Publications website at DOI: 10.1021/acs.inorgchem.5b00699.

■ AUTHOR INFORMATION

Corresponding Authors

*E-mail: kovacs@chem.washington.edu.
*E-mail: serena.debeer@cec.mpg.de.

Notes

The authors declare no competing financial interest.

■ ACKNOWLEDGMENTS

Michael Coggins is thanked for synthetic advice, and Vera Krewald is acknowledged for helpful discussion regarding the calculations. Stefan Hugenbruch and Sergey Peredkov are thanked for assistance with data collection. The authors gratefully acknowledge financial support from the Max-Planck-Gesellschaft (S.D.), the US National Institutes of Health (J.A.K., RO1GM45881), and the German Academic Exchange Service (graduate scholarship to J.A.R.) The ESRF is acknowledged for providing beamtime, and Pieter Glatzel is thanked for technical assistance with measurements.

■ REFERENCES

(1) Wallar, B. J.; Lipscomb, J. D. *Chem. Rev.* **1996**, *96*, 2625−2658.
(2) McEvoy, J. P.; Brudvig, G. W. *Chem. Rev.* **2006**, *106*, 4455−4483.
(3) Denisov, I. G.; Makris, T. M.; Sligar, S. G.; Schlichting, I. *Chem. Rev.* **2005**, *105*, 2253−2277.
(4) Que, L.; Tolman, W. B. *Nature* **2008**, *455*, 333−340.
(5) Park, G. Y.; Qayyum, M. F.; Woertink, J.; Hodgson, K. O.; Hedman, B.; Sarjeant, A. A. N.; Solomon, E. I.; Karlin, K. D. *J. Am. Chem. Soc.* **2012**, *134*, 8513−8524.
(6) Ogliaro, F.; de Visser, S. P.; Shaik, S. *J. Inorg. Biochem.* **2002**, *91*, 554−567.
(7) Roos, K.; Siegbahn, P. E. M. *J. Biol. Inorg. Chem.* **2012**, *17*, 363−373.
(8) Boal, A. K.; Cotruvo, J. A.; Stubbe, J.; Rosenzweig, A. C. *Biochemistry* **2012**, *51*, 3861−3871.
(9) Cotruvo, J. A.; Stubbe, J. *Biochemistry* **2011**, *50*, 1672−1681.
(10) Goldsmith, C. R.; Cole, A. P.; Stack, T. D. P. *J. Am. Chem. Soc.* **2005**, *127*, 9904−9912.
(11) Hamberg, M.; Su, C.; Oliw, E. *J. Biol. Chem.* **1998**, *273*, 13080−13088.
(12) Oliw, E. H.; Jernerén, F.; Hoffmann, I.; Sahlin, M.; Garscha, U. *Biochim. Biophys. Acta* **2011**, *1811*, 138−147.
(13) Bull, C.; Niederhoffer, E. C.; Yoshida, T.; Fee, J. A. *J. Am. Chem. Soc.* **1991**, *113*, 4069−4076.
(14) Wu, A. J.; Penner-Hahn, J. E.; Pecoraro, V. L. *Chem. Rev.* **2004**, *104*, 903−938.
(15) Sauer, K.; Yano, J.; Yachandra, V. K. *Photosynth. Res.* **2005**, *85*, 73−86.
(16) Umena, Y.; Kawakami, K.; Shen, J.-R.; Kamiya, N. *Nature* **2011**, *473*, 55−60.
(17) Coggins, M. K.; Sun, X.; Kwak, Y.; Solomon, E. I.; Rybak-Akimova, E.; Kovacs, J. A. *J. Am. Chem. Soc.* **2013**, *135*, 5631−5640.
(18) Coggins, M. K.; Toledo, S.; Shaffer, E.; Kaminsky, W.; Shearer, J.; Kovacs, J. A. *Inorg. Chem.* **2012**, *51*, 6633−6644.
(19) Coggins, M. K.; Martin-Diaconescu, V.; DeBeer, S.; Kovacs, J. A. *J. Am. Chem. Soc.* **2013**, *135*, 4260−4272.
(20) Ray, K.; Pfaff, F. F.; Wang, B.; Nam, W. *J. Am. Chem. Soc.* **2014**, *136*, 13942−13958.
(21) Yin, G. *Acc. Chem. Res.* **2013**, *46*, 483−492.
(22) Kern, J.; Alonso-Mori, R.; Tran, R.; Hattne, J.; Gildea, R. J.; Echols, N.; Glöckner, C.; Hellmich, J.; Laksmono, H.; Sierra, R. G.; Lassalle-Kaiser, B.; Koroidov, S.; Lampe, A.; Han, G.; Gul, S.; Difiore, D.; Milathianaki, D.; Fry, A. R.; Miahnahri, A.; Schafer, D. W.; Messerschmidt, M.; Seibert, M. M.; Koglin, J. E.; Sokaras, D.; Weng, T.-C.; Sellberg, J.; Latimer, M. J.; Grosse-Kunstleve, R. W.; Zwart, P. H.; White, W. E.; Glatzel, P.; Adams, P. D.; Bogan, M. J.; Williams, G. J.; Boutet, S.; Messinger, J.; Zouni, A.; Sauter, N. K.; Yachandra, V. K.; Bergmann, U.; Yano, J. *Science* **2013**, *340*, 491−495.
(23) Pushkar, Y.; Long, X.; Glatzel, P.; Brudvig, G. W.; Dismukes, G. C.; Collins, T. J.; Yachandra, V. K.; Yano, J.; Bergmann, U. *Angew. Chem., Int. Ed.* **2010**, *49*, 800−803.
(24) Berthold, T.; Gromoff, E. D.; Von Santabarbara, S.; Stehle, P.; Link, G.; Poluektov, O. G.; Heathcote, P.; Beck, C. F.; Thurnauer, M. C.; Kothe, G. *J. Am. Chem. Soc.* **2012**, *134*, 5563−5576.
(25) Kuzek, D.; Pace, R. J. *Biochim. Biophys. Acta* **2001**, *1503*, 123−137.
(26) Penner-Hahn, J. E. *Coord. Chem. Rev.* **2005**, *249*, 161−177.
(27) Atkins, A. J.; Bauer, M.; Jacob, C. R. *Phys. Chem. Chem. Phys.* **2013**, *15*, 8095−8105.
(28) Lancaster, K. M.; Roemelt, M.; Ettenhuber, P.; Hu, Y.; Ribbe, M. W.; Neese, F.; Bergmann, U.; DeBeer, S. *Science* **2011**, *334*, 974−977.
(29) Leto, D. F.; Jackson, T. A. *Inorg. Chem.* **2014**, *53*, 6179−6194.
(30) Bergmann, U.; Horne, C. R.; Collins, T. J.; Workman, J. M.; Cramer, S. P. *Chem. Phys. Lett.* **1999**, *302*, 119−124.
(31) De Groot, F. *Chem. Rev.* **2001**, *101*, 1779−1808.
(32) Glatzel, P.; Bergmann, U. *Coord. Chem. Rev.* **2005**, *249*, 65−95.
(33) Lassalle-Kaiser, B.; Boron, T. T., III; Krewald, V.; Kern, J.; Beckwith, M. A.; Delgado-Jaime, M. U.; Schroeder, H.; Alonso-Mori, R.; Nordlund, D.; Weng, T.-C.; Sokaras, D.; Neese, F.; Bergmann, U.; Yachandra, V. K.; DeBeer, S.; Pecoraro, V. L.; Yano, J. *Inorg. Chem.* **2013**, *52*, 12915−12922.
(34) Beckwith, M. A.; Roemelt, M.; Collomb, M.-N.; DuBoc, C.; Weng, T.-C.; Bergmann, U.; Glatzel, P.; Neese, F.; DeBeer, S. *Inorg. Chem.* **2011**, *50*, 8397−8409.
(35) Chandrasekaran, P.; Chiang, K.; Nordlund, D.; Bergmann, U.; Holland, P. L.; DeBeer, S. *Inorg. Chem.* **2013**, *52*, 6286−6298.
(36) Pollock, C. J.; Delgado-Jaime, M. U.; Atanasov, M.; Neese, F.; DeBeer, S. *J. Am. Chem. Soc.* **2014**, *136*, 9453.

DOI: 10.1021/acs.inorgchem.5b00699
Inorg. Chem. 2015, 54, 6410−6422

(37) Pollock, C. J.; DeBeer, S. *J. Am. Chem. Soc.* **2011**, *133*, 5594−5601.
(38) Lee, N.; Petrenko, T.; Bergmann, U.; Neese, F.; DeBeer, S. *J. Am. Chem. Soc.* **2010**, *132*, 9715−9727.
(39) Smolentsev, G.; Soldatov, A. V.; Messinger, J.; Merz, K.; Weyhermüller, T.; Bergmann, U.; Pushkar, Y.; Yano, J.; Yachandra, V. K.; Glatzel, P. *J. Am. Chem. Soc.* **2009**, *131*, 13161−13167.
(40) Pollock, C. J.; Grubel, K.; Holland, P. L.; DeBeer, S. *J. Am. Chem. Soc.* **2013**, *135*, 11803−11808.
(41) Krewald, V.; Lassalle-Kaiser, B.; Boron, T. T., III; Pollock, C. J.; Kern, J.; Beckwith, M. A.; Yachandra, V. K.; Pecoraro, V. L.; Yano, J.; Neese, F.; DeBeer, S. *Inorg. Chem.* **2013**, *52*, 12904−12914.
(42) Roemelt, M.; Beckwith, M. A.; Duboc, C.; Collomb, M.-N.; Neese, F.; DeBeer, S. *Inorg. Chem.* **2012**, *51*, 680−687.
(43) Solé, V. A.; Papillon, E.; Cotte, M.; Walter, P.; Susini, J. *Spectrochim. Acta, Part B* **2007**, *62*, 63.
(44) Neese, F. *Wiley Interdiscip. Rev. Comput. Mol. Sci.* **2012**, *2*, 73.
(45) Lenthe, E. V.; Avoird, A. V. D.; Wormer, P. E. S. *J. Chem. Phys.* **1998**, *109*, 392.
(46) Grimme, S.; Ehrlich, S.; Goerigk, L. *J. Comput. Chem.* **2011**, *32*, 1456.
(47) Grimme, S.; Antony, J.; Ehrlich, S.; Krieg, H. *J. Chem. Phys.* **2010**, *132*, 154104.
(48) Pantazis, D. A.; Chen, X. Y.; Landis, C. R.; Neese, F. *J. Chem. Theory Comput.* **2008**, *4*, 908.
(49) Klamt, A.; Schüürmann, G. *J. Chem. Soc., Perkin Trans. 2* **1993**, *5*, 799.
(50) Becke, A. . *Phys. Rev. A* **1988**, *38*, 3098.
(51) Perdew, J. P. *Phys. Rev. B* **1986**, *33*, 8822.
(52) Weigend, A. *Phys. Chem. Chem. Phys.* **2006**, *8*, 1057.
(53) Hess, B. A.; Marian, C. M.; Wahlgren, U.; Gropen, O. *Chem. Phys. Lett.* **1996**, *251* (5−6), 365.
(54) Hirata, S.; Head-Gordon, M. *Chem. Phys. Lett.* **1999**, *314*, 291−299.
(55) Neese, F.; Olbrich, G. *Chem. Phys. Lett.* **2002**, *362*, 170−178.
(56) Dunlap, B. I.; Connolly, J. W. D.; Sabin, J. R. *J. Chem. Phys.* **1979**, *71*, 3396−3402.
(57) Feyereisen, M.; Fitzgerald, G.; Komornicki, A. *Chem. Phys. Lett.* **1993**, *208*, 359−363.
(58) Neese, F.; Wennmohs, F.; Hansen, A.; Becker, U. *Chem. Phys.* **2009**, *356*, 98−109.
(59) Delgado-Jaime, M. U.; DeBeer, S. *J. Comput. Chem.* **2012**, *33*, 2180−2185.
(60) Pettersen, E. F.; Goddard, T. D.; Huang, C. C.; Couch, G. S.; Greenblatt, D. M.; Meng, E. C.; Ferrin, T. E. *J. Comput. Chem.* **2004**, *13*, 1605.
(61) Bauer, M. *Phys. Chem. Chem. Phys.* **2014**, *16*, 13827−13837.
(62) Hayashi, H.; Udagawa, Y.; Caliebe, W. A.; Kao, C.-C. *Chem. Phys. Lett.* **2003**, *371*, 125−130.
(63) Delgado-Jaime, M. U.; DeBeer, S.; Bauer, M. *Chem.—Eur. J.* **2013**, *19*, 15888−15897.
(64) Yamanaka, S.; Kawakami, T.; Nagao, H.; Yamaguchi, K. *Chem. Phys. Lett.* **1994**, *231*, 25−33.
(65) Lima, F. A.; Bjornsson, R.; Weyhermüller, T.; Chandrasekaran, P.; Glatzel, P.; Neese, F.; DeBeer, S. *Phys. Chem. Chem. Phys.* **2013**, *15*, 20911−20920.
(66) MacNaughton, J. B.; Näslund, L.-A.; Anniyev, T.; Ogasawara, H.; Nilsson, A. *Phys. Chem. Chem. Phys.* **2010**, *12*, 5712−5716.
(67) Kovacs, J.; Brines, L. *Acc. Chem. Res.* **2007**, *40*, 501−509.
(68) Leto, D. F.; Jackson, T. A. *J. Biol. Inorg. Chem.* **2014**, *19*, 1−15.
(69) Seo, M. S.; Kim, J. Y.; Annaraj, J.; Kim, Y.; Lee, Y.-M.; Kim, S.-J.; Kim, J.; Nam, W. *Angew. Chem., Int. Ed.* **2007**, *46*, 377−380.
(70) Pollock, C. J.; Lancaster, K. M.; Finkelstein, K. D.; DeBeer, S. *Inorg. Chem.* **2014**, *53*, 10378−10385.

DOI: 10.1021/acs.inorgchem.5b00699
Inorg. Chem. 2015, 54, 6410−6422